



Amorphous Ni(III)-based sulfides as bifunctional water and urea oxidation anode electrocatalysts for hydrogen generation from urea-containing water

Xin Jia^a, Hongjun Kang^{a,b}, Xiaoxuan Yang^c, Yunlong Li^a, Kai Cui^b, Xiaohong Wu^{a,b,**}, Wei Qin^{a,*}, Gang Wu^{c,*}

^a School of Materials Science and Engineering, Harbin Institute of Technology, Harbin, Heilongjiang 150001, China

^b School of Chemistry and Chemical Engineering, Harbin Institute of Technology, Harbin, Heilongjiang 150001, China

^c Department of Chemical and Biological Engineering, University at Buffalo, The State University of New York, Buffalo, NY 14260, USA

ARTICLE INFO

Keywords:

in situ electrochemical tuning
Water electrolysis
Oxygen evolution reaction
Urea oxidation reaction

ABSTRACT

It is highly desired to design high-performance bifunctional electrocatalysts for an efficient oxygen evolution reaction (OER) and urea oxidation reaction (UOR) as anode water electrolysis reactions, which can be used for hydrogen production by using urea-containing water. Herein, a novel electrocatalyst composed of amorphous Ni(OH)S nanosheets was prepared by hydrolysis of $\text{NiCl}_2(\text{CH}_3\text{CSNH}_2)_4$ at room temperature. From spectroscopic characterization and density functional theory (DFT) calculations, the Ni(OH)S catalyst contains a Ni^{3+} -rich phase, which can significantly accelerate the reaction kinetics. The anode electrocatalyst shows excellent OER activity, generating 10 mA cm^{-2} with only 250 mV overpotentials. When employed as a UOR anode, it could reach 10 mA cm^{-2} at 1.34 V, 140 mV lower than OER. Notably, the Ni(OH)S/NF anode exhibits decent bifunctional UOR and OER activities and presents the lowest overpotentials compared to a NiFe-PBA/NF UOR catalyst and a typical RuO_2 /NF OER catalyst. This work provides a novel strategy for synthesizing amorphous Ni(III)-based sulfides nanosheets for bifunctional OER/UOR electrocatalysts, which is significant for efficient and stable hydrogen production by using urea-containing wastewater.

1. Introduction

Hydrogen is highly expected to be a substitute for traditional fossil fuel energy because of its high calorific density and environmental friendliness [1]. Among a variety of hydrogen production methods, water splitting to produce hydrogen shows high efficiency and product purity, attracting increasing interest [2]. However, as the paramount half-reaction of water splitting, the oxygen evolution reaction (OER) occurring at the anode is a complicated four-electron-transfer process with sluggish kinetics, seriously impeding its application in industrial hydrogen production [3]. Alternatively, the urea oxidation reaction (UOR) has attracted considerable attention in recent years, which could mitigate the OER overpotential as the more favored half-reaction during the electrolysis of water by using urea-rich wastewater. The much lower thermodynamic potential of the UOR (0.37 V) vs. OER (1.23 V) can significantly enhance the efficiency for H_2 generation via water electrolysis [4–6]. However, the UOR also suffered from slow reaction

kinetics with a complex six-electron-transfer process [7]. Highly active and stable electrocatalysts, therefore, are required to simultaneously overcome the sluggish kinetics of both reactions.

It should be noted that urea in living sewage and industrial wastewater is prevalent. Therefore, designing a bifunctional electrocatalyst for both OER and UOR is essential for hydrogen production with low energy consumption [8]. Over the past decades, some noble metal-based catalysts (RuO_2 and IrO_2 for the OER; Pt and Pd for the UOR) have been commonly used due to their prominent electrocatalytic activities. However, their scarcity, high cost, and single-function hinder their large-scale applications [9,10]. Therefore, it is essential to explore nonprecious metal bifunctional catalysts for high-performance OER and UOR to substitute noble metal-based counterparts toward clean hydrogen generation.

Recently, a deluge of 3d transition metal compounds (TMCs), including Ni, has been extensively studied as high-efficiency OER electrocatalysts [11–14]. Also, the known electrocatalysts used for the UOR

* Corresponding author at: School of Materials Science and Engineering, Harbin Institute of Technology, Harbin, Heilongjiang 150001, China.

** Corresponding authors.

E-mail addresses: wuxiaohong@hit.edu.cn (X. Wu), qinwei@hit.edu.cn (W. Qin), gangwu@buffalo.edu (G. Wu).

are mainly Ni derivatives, such as alloys, hydroxides, oxides, and sulfides [15,16]. Therefore, Ni-based catalysts could be promising candidates for effective and stable bifunctional OER/UOR catalysts. Ni has eight electrons in the 3d electron orbital that provide the basis for its unique electrocatalytic properties. According to the molecular orbital principles, the e_g orbital occupancy determines the binding strength with oxygen-containing intermediates, i.e., the lower the e_g occupancy, the stronger binding of oxygen. It is well known that the OER process involves the adsorption of OH⁻, along with the desorption of O₂, which requires the OER catalyst with a medium adsorption strength for active intermediate species [17]. Besides, the number of e_g electrons should be as close to 1. Therefore, the Ni³⁺(3d⁷) species with an electronic configuration of $t_{2g}^6e_g^1$ are considered as potential highly active catalysts for the OER [18,19]. Furthermore, the mechanism for the UOR on Ni (II)-based catalysts in alkaline electrolytes indicates that the Ni(II)-based catalysts inevitably undergo a self-oxidation process, forming the Ni³⁺ derivative on the surfaces (which always happens at ~1.36 V), and serving as direct active sites (i.e., NiOOH) for the UOR [20,21]. A widely studied UOR pathway is $6\text{Ni}^{3+}\text{OOH} + \text{CO}(\text{NH}_2)_2 + 6\text{OH}^- \rightarrow 6\text{Ni}^{2+}(\text{OH})_2 + \text{N}_2 + \text{CO}_2 + 5\text{H}_2\text{O} + 6\text{e}^-$. Based on the above understanding, constructing Ni³⁺ catalysts may efficiently catalyze both OER and UOR [22, 23].

Nevertheless, the relatively low electrical conductivity of those directly synthesized NiOOH catalysts may limit catalytic performance [24]. In contrast, the *in-situ* reconstructed NiOOH via electrochemical methods usually exhibits higher catalytic performance than their directly synthesized counterparts because of its abundant defects and low-crystalline structure [25]. Therefore, various nickel sulfide-based materials [24,26–28], such as Ni₂S₃, Ni₃S₄, Ni₉S₈, and NiCo₂S₄, have been developed to achieve high electrocatalytic performance due to their diverse valence states, high electrical conductivity, and rapid *in-situ* electrochemical reconstruction. However, the *in-situ* electrochemical reconstructions usually occur at the surface of these metal sulfides, resulting in large amounts of inert species buried in the core, which cannot participate in catalysis [29,30]. A recent report shows that the amorphous structure of the electrocatalysts can significantly affect its *in situ* electrochemical reconstructions [31]. The prominent advantage of an amorphous structure is the disordered arrangement with abundant defects and dangling bonds, which could improve structural flexibility and facilitate the reconstruction of the electrocatalysts to the (oxy)hydroxide phase during the OER and UOR processes. Hence, we speculate if Ni(III)-based sulfide catalysts have an amorphous structure, they will entirely reconstruct into the actual active phase (NiOOH) during *in situ* electrochemical tunings and display appealing OER and UOR performance. Currently, the facile synthesis of amorphous Ni (III)-based sulfides bifunctional OER/UOR electrocatalysts is challenging and rarely reported.

Herein, we reported a simple and effective strategy to synthesize an amorphous Ni(III)-based sulfide electrocatalyst as a bifunctional catalyst for the OER and UOR. Firstly, a NiCl₂(CH₃CSNH₂)₄ metal complex (Ni-TAA) was synthesized by a facile complexation reaction, where the center metal (Ni) was coordinated with four sulfur atoms from organic linkers (thioacetamide) and two chlorine atoms in trans apical positions, showing a highly symmetrical octahedral structure. The Ni-TAA metal complexes are unstable in water and can be hydrolyzed to form amorphous sulfide nanosheets, in which the valence state of Ni is +3, named Ni(OH)S. The *in situ* formed amorphous Ni(OH)S nanosheets can manifest superior OER and UOR performance. It only requires a low overpotential of 250 mV for generating O₂ at 10 mA cm⁻² in 1.0 M KOH solution, and the Tafel slope is only 51 mV dec⁻¹. At the same time, it is applied to urea oxidation in an electrolyte containing 1.0 M KOH and 0.33 M urea. It presents a low potential of 1.34 V to obtain a current density of 10 mA cm⁻², about 140 mV lower than its OER. The Ni(OH)S/NF electrode has the lowest power consumption under the same hydrogen production volume than a well-known NiFe-PBA/NF UOR catalyst and a RuO₂/NF OER catalyst. Operando electrochemical

impedance spectroscopy (EIS) and *in situ* Raman spectra were utilized to study the reaction interfaces during the OER and the UOR.

2. Experimental section

2.1. Catalyst synthesis

During the synthesis of NiCl₂(CH₃CSNH₂)₄ precursor, 9.02 g (120 mmol) of thioacetamide (TAA) and 7.13 g of NiCl₂ were dissolved in 200 mL of ethanol under stirring at room temperature for 60 min, and the NiCl₂(CH₃CSNH₂)₄ (Ni-TAA) was obtained after aging at room temperature for 12 h. The produced solids were collected by centrifugation at 9000 rpm for 5 min, washed with ethanol three times, and dried at 60 °C for 24 h. These experiments were all performed in the air.

As for the synthesis of Ni(OH)S, 10 g of the as-synthesized Ni-TAA NPs were dispersed in 100 mL deionized water by sonication for 15 min, and Ni(OH)S particles were obtained after aging at room temperature for 24 h. The produced solids were collected by centrifugation at 9000 rpm for 5 min, washed with ethanol three times, and dried at 60 °C for 24 h.

Finally, the as-synthesized Ni(OH)S was further annealed in N₂ at 350 °C with 5 °C min⁻¹ for 5 h. The obtained products were named Ni (OH)S-350. The Ni(OH)S/NF electrode was prepared on nickel foam (NF) (2 × 2 cm²) by using the identical methods described above.

2.2. Physical Characterization

Powder XRD patterns were recorded on an Empyrean X-ray diffractometer equipped with a Cu Kα radiation source (λ = 0.154178 nm). XPS measurements were performed using a Thermo Fischer ESCALAB 250Xi spectrophotometer with the excitation source of monochromatic aluminum. The structure and composition of the samples were studied by scanning electron microscopy (Merlin Compact SEM operated at 10–20 kV) and transmission electron microscopy (Tecnai G2 F30 TEM operated at 200 kV) along with energy-dispersive X-ray spectroscopy (EDS) for both SEM and TEM. Fourier transform infrared spectroscopy (FTIR) data were acquired using a Nexus system. Raman spectra were acquired using a NANOFINDER spectrometer with 532 nm of the laser source wavelength. *In situ* Raman measurements were carried out using a NANOFINDER spectrometer with the measured potential for the OER and UOR was in the range of 1.25–1.60 V controlled by an electrochemical workstation (CHI660E Instruments). The *in situ* electrochemical three-electrode cells contained Ni(OH)S/NF as the working electrode, Ag/AgCl as the reference electrode, and Pt wire as the counter electrode.

2.3. Computing methods

Our *ab initio* density functional theory calculations (DFT) use projector augmented wave to describe the core electrons and the generalized gradient approximation with the Perdew-Burke-Ernzerhof functional, as implemented in VASP (Vienna *Ab initio* Simulation Package) code. For the structure relaxation of thioacetamide and NiCl₂(CH₃CSNH₂)₄, the kinetic energy cutoff for the plane-wave basis is set to 400 eV. All the structures are fully relaxed until the force on each atom is less than 0.01 eV/Å. The van der Waals interaction (vdW) is calculated by employing the DFT-D3 method. Furthermore, the cutoff energy is 400 eV, and the full geometry optimizations are carried out with the convergence thresholds of 10⁻⁴ eV for Ni(OH)S.

2.4. Electrochemical measurements

Linear sweep voltammetry (LSV), chronopotentiometry (CP), and cyclic voltammetry (CV) measurements were carried out in a 1.0 M KOH for the OER and 1.0 M KOH + 0.33 M urea for the UOR using a potentiostat (CHI660D, CH Instruments). All measurements were performed

in a three-electrode configuration at room temperature, using a saturated calomel electrode as the reference electrode and a graphite rod as the counter electrode. An electrochemical activation process was firstly scanned in CV from 0 to 0.7 V (vs. SCE) at a rate of 0.1 V/s for 40 cycles. All potential measurements were converted to the RHE based on the following formula $E_{\text{RHE}} = E_{\text{SCE}} + 0.242 + 0.059 \text{ pH}$ (in volts). The overpotentials for the OER were calculated according to the following formula: $\eta = E_{\text{RHE}} - 1.23 \text{ V}$. The electrochemical double-layer capacitance was determined from CV curves measured in the potential range according to the following equation: $C_{\text{dl}} = I_c/\nu$, where C_{dl} , I_c , and ν are the double-layer capacitance (mF cm^{-2}) of the electroactive materials, charging current (mA cm^{-2}), and scan rate (mV s^{-1}), respectively. For the LSV measurements, the potential was swept from 1.0 to 1.7 V (vs. RHE) at a scan rate of 5 mV s^{-1} . The Faradic efficiency of electrocatalysts was estimated by collecting the amount of oxygen produced by continuous electrolysis at 20 mA cm^{-2} for about 4000 s using a volumetric method (V_{actual}). Then, the theoretical generated O_2 volumes values ($V_{\text{theoretical}}$) were calculated by Faraday's law of electrolysis ($Q = zn_{\text{O}_2}F$) and Ideal Gas Law ($PV_{\text{O}_2} = n_{\text{O}_2}RT$). Finally, the Faradaic efficiency was obtained by comparing the actual volume of oxygen evolution with the theoretical one: $\text{FE} = V_{\text{actual}}/V_{\text{theoretical}}$. Chronopotentiometry was used to evaluate the catalytic stability; the current densities were set to 10 and 50 mA cm^{-2} . The potentials were limited to 1.4–2.0 V (vs. RHE). Operando EIS was recorded at 1.25–1.60 V (vs. RHE) using an AC voltage amplitude of 2 mV and a quiet time of 5 s. The frequency range investigated was from 10 k to 0.01 Hz.

3. Results and discussion

3.1. Synthesis and structural characterization

The Ni-TAA precursor was synthesized via the complexation of TAA and NiCl_2 in an ethanol solution (Fig. 1a). It was reported that Ni-TAA could have a similar trans-octahedral structure to $(\text{H}_2\text{O})_4\text{NiCl}_2$, $(\text{TMeT})_4\text{NiCl}_2$, and the dimorphic forms of $(\text{ETU})_4\text{NiCl}_2$ [32]. DFT

calculations predicted that the Ni-TAA is octahedral with a high symmetry and is not easy to produce the Jahn-Teller effect on the atomic scale, resulting in the primary Ni^{2+} . The electronic configuration of Ni-TAA is $t_{2g}^6e_g^2$ (see the detailed phase and crystal structure analysis in Figs. S1–S2). In addition, the Ni-TAA metal complex can be hydrolyzed by water, showing inevitable destabilization. As shown in Fig. 1b–d, the hydrolyzed product was composed of an average size of $\sim 200 \text{ nm}$ amorphous nanosheets from the high-resolution transmission electron microscopy (HR-TEM) image and a broad ring SAED pattern (inset of Fig. 1d). Energy-dispersive X-ray spectroscopy (EDS) mapping images (Fig. 1e–h) showed that the main elements distributed in the amorphous nanosheets were Ni, S, and O.

3.2. Spectroscopic characterization analysis

A series of spectroscopic characterizations were used to measure the new-formed sample to determine Ni-TAA compositions after the critical hydrolysis. The crystal information of hydrolyzed product was analyzed using the powder X-ray diffraction (XRD), indicating its dominant amorphous phase (Fig. 2a). After the controlled annealing treatment at 350°C under N_2 , the crystallographic phase of the annealed products could be identified as $\text{Ni}_{0.96}\text{S}$ (JCPDS card no. 50–1791), with no additional signals from possible impurities. Combined with the above EDS characterizations, the substance after hydrolysis can be identified as an amorphous Ni-based sulfide. X-ray photoelectron spectroscopy (XPS) was carried out to further investigate the electronic state (Figs. 2b, c, and S3). Regarding the valence state of Ni ions, the Ni spectra usually showed two doublet characteristics of Ni^{2+} and Ni^{3+} , which were assigned to the peaks at binding energies of 855.7 and 856.8 eV, respectively [33,34]. Interestingly, as shown in Fig. 2b, the Ni spectra of Ni-TAA only showed the peak of Ni^{2+} , which is consistent with the above analysis. In contrast, after hydrolysis, the sample showed the peak of Ni^{3+} , which means that an oxidation process accompanies the hydrolysis process. In the S 2p spectrum of the hydrolyzed product (Fig. 2c), the peak at 164.5 eV was typically a metal-sulfur (Ni-S) bond in the sulfide

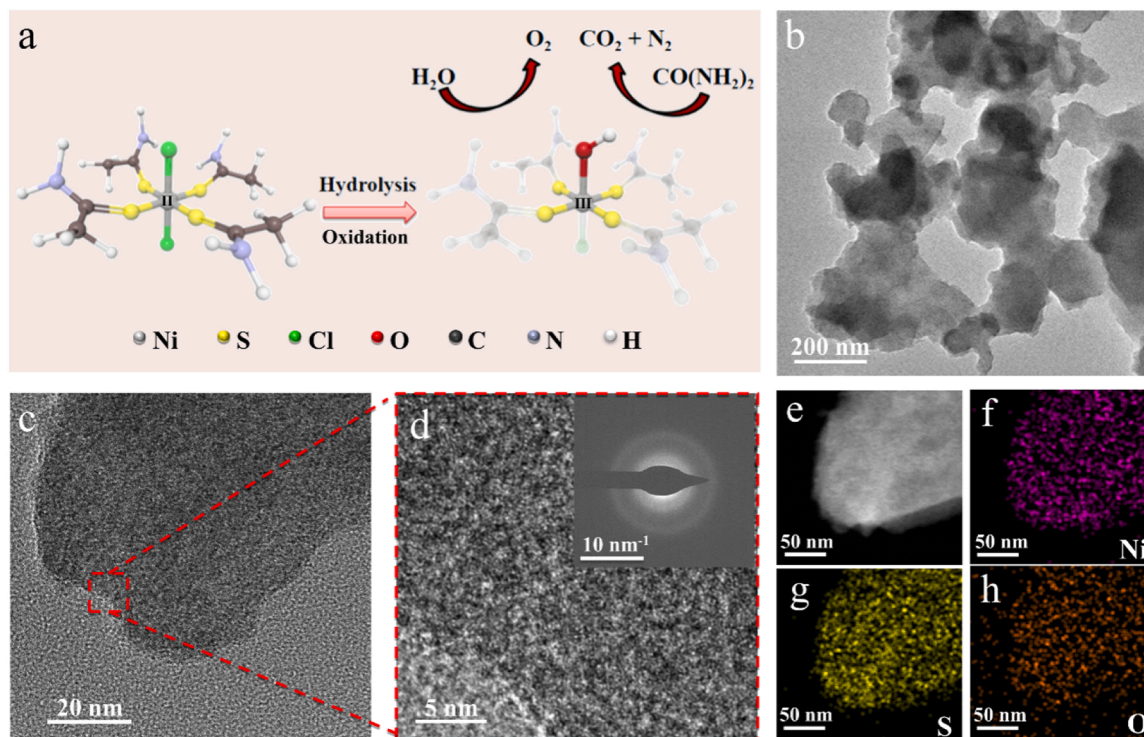


Fig. 1. (a) Schematics illustrating the atomic changes during hydrolysis. (b) Low and (c) high magnification TEM images of the Ni(OH)S, (d) HR-TEM image, and the SAED of the Ni(OH)S. (e–h) EDS elemental mapping of Ni(OH)S.

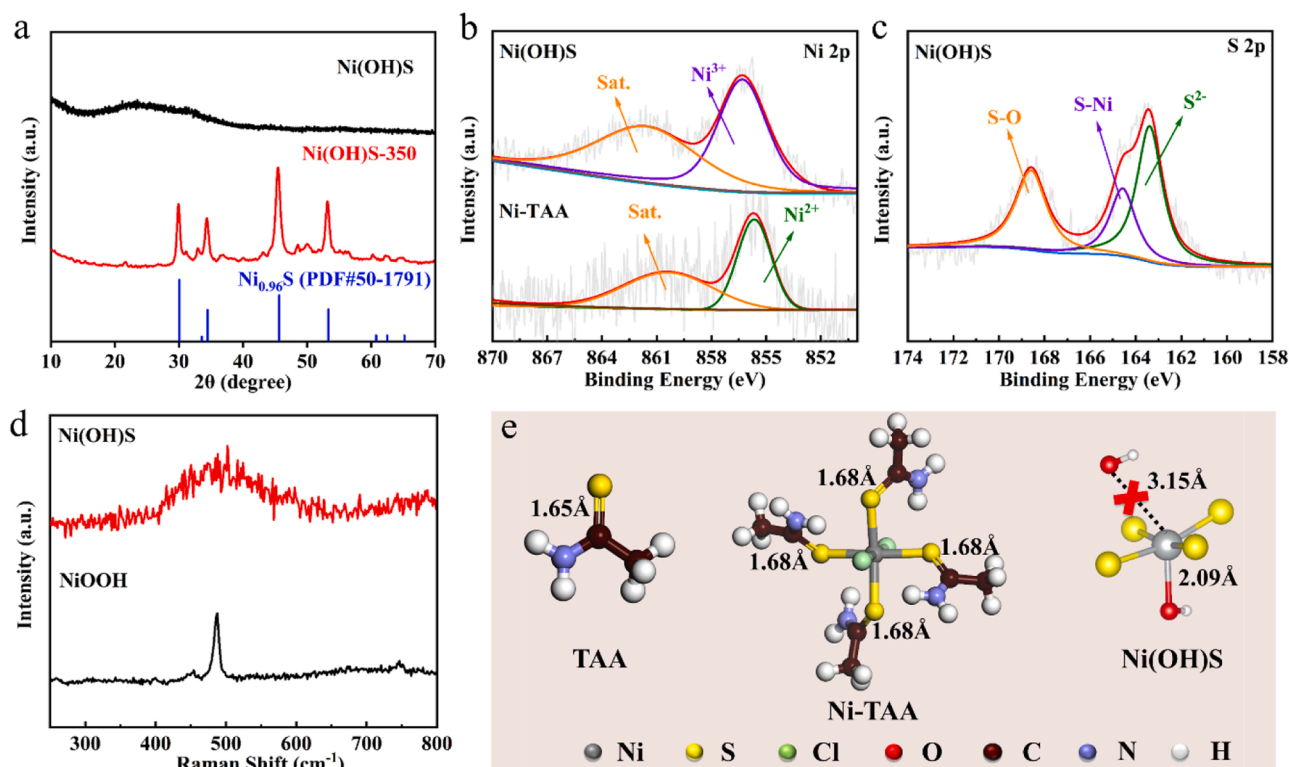


Fig. 2. (a) XRD patterns of Ni(OH)S and Ni(OH)S-350. Regional XPS spectra of (c) Ni 2p of Ni-TAA and Ni(OH)S and (d) S 2p of Ni(OH)S. (d) Raman spectra of Ni(OH)S and NiOOH. (e) The structure change of TAA, Ni-TAA, and Ni(OH)S.

material. In addition, the peak located at 168.8 eV could be assigned to the oxidized S species [33,34]. The Raman spectra of the hydrolyzed product exhibit a prominent peak at 490 cm⁻¹, corresponding to the lattice translational mode of NiOOH (Fig. 2d) [35,36]. Fourier transform infrared (FT-IR) spectroscopy in 3500–500 cm⁻¹ was carried out to detect its functional groups (Fig. S4a). Only a broad peak appeared at 1101 cm⁻¹, which was classified as a vibrational stretching mode of the Ni-OH group [37–39]. Combined with the above spectroscopic characterizations, we speculate the amorphous material could be Ni(OH)S.

To further explore the hydrolysis process of the Ni-TAA precursor, FT-IR, XPS, and DFT calculations were carried out to detect the changes in their functional groups and composition. As shown in FT-IR spectroscopy (Fig. S4a), the functional groups of the Ni-TAA metal complex were essentially the same as that of pure TAA, except for a new peak at around 656 cm⁻¹ representing the Ni-S bond of Ni-TAA. Moreover, the wavenumber of the C=S bond increases and its apparent redshift indicates that the S atoms in TAA were coordinated to Ni atoms and the newly formed strong interactions between them. These functional groups disappeared after the hydrolysis of Ni-TAA. XPS analyzed the compositions of the Ni-TAA and the Ni-TAA after hydrolysis, and the results (Fig. S3) are consistent with those from the EDS mapping. To analyze the hydrolysis process of the Ni-TAA, the pH and FT-IR spectroscopy of the solution before and after hydrolysis were analyzed (Fig. S4b, S5). The solution became acidic after the hydrolysis, and the FT-IR spectroscopy identified most of the functional groups of the Ni-TAA except for NH₂ and Ni-S (TAA), which means that the OH⁻ of the solution was consumed and participated in the hydrolysis reaction. Therefore, the likely Ni-TAA hydrolysis follows the equation (CH₃CSNH₂ + 3OH⁻ → CH₃COO⁻ + NH₃ + S²⁻ + H₂O). The reason is that NiCl₂ coordinates with TAA, leading to the extension of the C=S bond of Ni-TAA, and the bond length of the C=S bond increases from 1.65 to 1.68 Å (Fig. 2e). The elongated C=S bond in the Ni-TAA is much weaker than others, which can be destroyed. Only Ni-S bonds are retained. In addition, NiCl₂ is usually hydrolyzed to form Ni(OH)₂ in an alkaline

solution. However, the material's structure after hydrolysis was predicted by DFT calculations, and the results showed that Ni could only connect to one OH (Fig. 2e). This shows that the hydrolysis process is accompanied by the oxidation process, resulting in the change of the valence state of Ni.

3.3. Electrocatalytic OER and UOR performances

As mentioned above, amorphous nanomaterials usually exhibit superior performance toward OER, in which the Ni³⁺ site could accelerate the catalytic reaction [17,31]. To determine the electrocatalytic activity of the amorphous Ni(OH)S for the OER, a traditional three-electrode cell was set up with a 1.0 M KOH solution as the electrolytes. For a comparison, NiMoO₄/NF [23], and NiFe-PBA/NF [40], with the best UOR performance reported, and the commonly used OER RuO₂ catalyst was also measured under the same conditions. A Ni(OH)S/NF catalyst was prepared on the nickel foam via a self-assembly method (Fig. S6). A series of characterization tests such as SEM, TEM, FT-IR, Raman spectra, and XPS were carried out to characterize the Ni(OH)S/NF electrode (Figs. S7–S8). The uniform distribution of Ni, S, and O at the surface of NF can be seen from Fig. S8, and the self-assembled synthesized material on the NF has the same properties as the standalone Ni(OH)S powder, indicating the formation of Ni(OH)S/NF. The prepared Ni(OH)S on Ni foam (1 cm²) served directly as the working electrode with a loading of 5 mg cm⁻². The LSV curves in Fig. 3a exhibited that the Ni(OH)S/NF catalyst has the lowest overpotential for the OER with a value of ~250 mV to reach the benchmark current density of 10 mA cm⁻². In comparison, the overpotentials for bare Ni foam, RuO₂/NF, NiFe-PBA/NF, and NiMoO₄/NF electrocatalysts were ~375, ~310, ~285, and ~274 mV, respectively, much higher than Ni(OH)S/NF. A significant oxidation curve was observed before oxygen evolution at the potential of 1.4 V. Traditional Ni²⁺ based catalysts such as NiFe-PBA and NiMoO₄, Ni²⁺ is often oxidized to Ni³⁺ at the potential of 1.35 V to trigger the OER process. The higher potential oxidation of Ni(OH)S

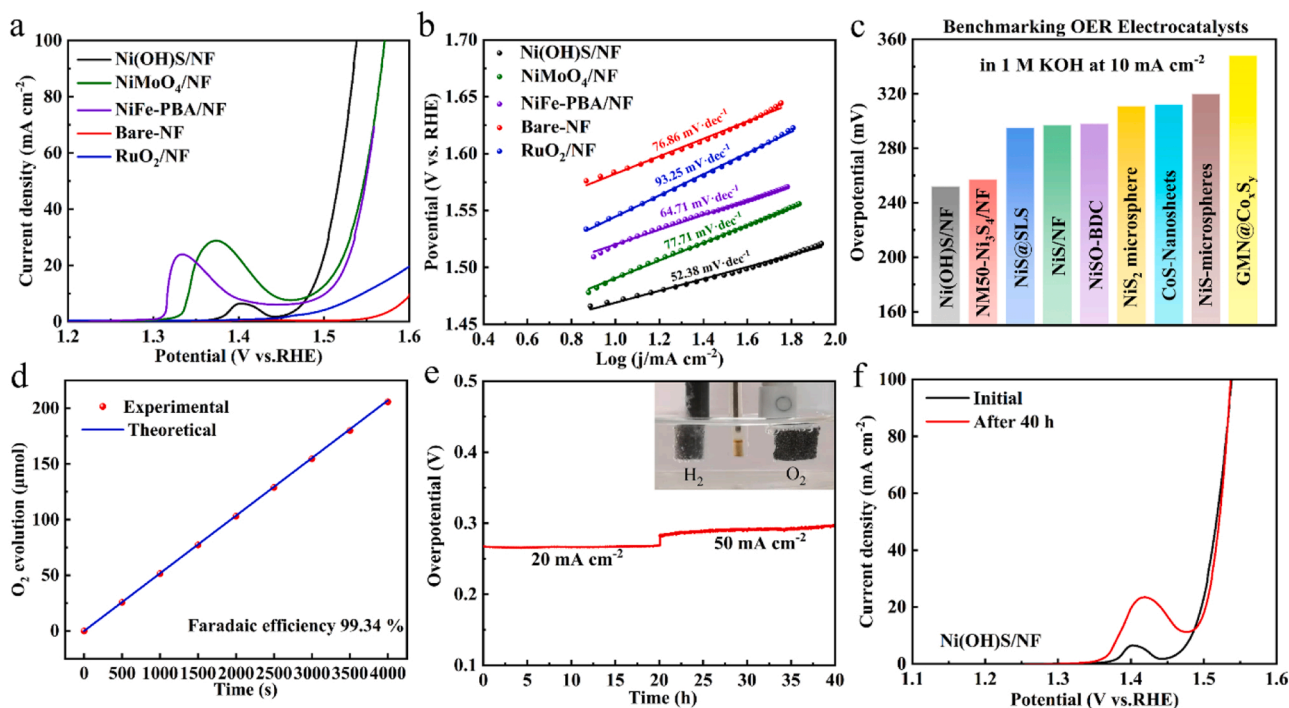


Fig. 3. (a) LSV curves, and (b) Tafel plots of Ni(OH)S/NF, NiMoO₄/NF, NiFe-PBA/NF, RuO₂/NF, and bare Ni foam in 1.0 M KOH at 5 mV s⁻¹. (c) The overpotential at 10 mA cm⁻² compared to other recently reported catalysts. (d) Faradaic efficiency of Ni(OH)S/NF at 20 mA cm⁻². (e) The chronoamperometry curve of Ni(OH)S/NF at a current density of 20 mA cm⁻² and 50 mA cm⁻² for 40 h. (f) LSV of Ni(OH)S/NF before and after 40 h of OER.

indicates that the Ni³⁺ based catalyst will be oxidized to a higher valence state to trigger the OER process. The Tafel slope was carried out to further investigate the kinetic properties of these catalysts, which were

strongly linked to the rate of the electrocatalytic reaction (Fig. 3b). The Tafel slope for the amorphous Ni(OH)S catalyst was 51 mV dec⁻¹, which is much lower than those of the control catalysts, indicating the

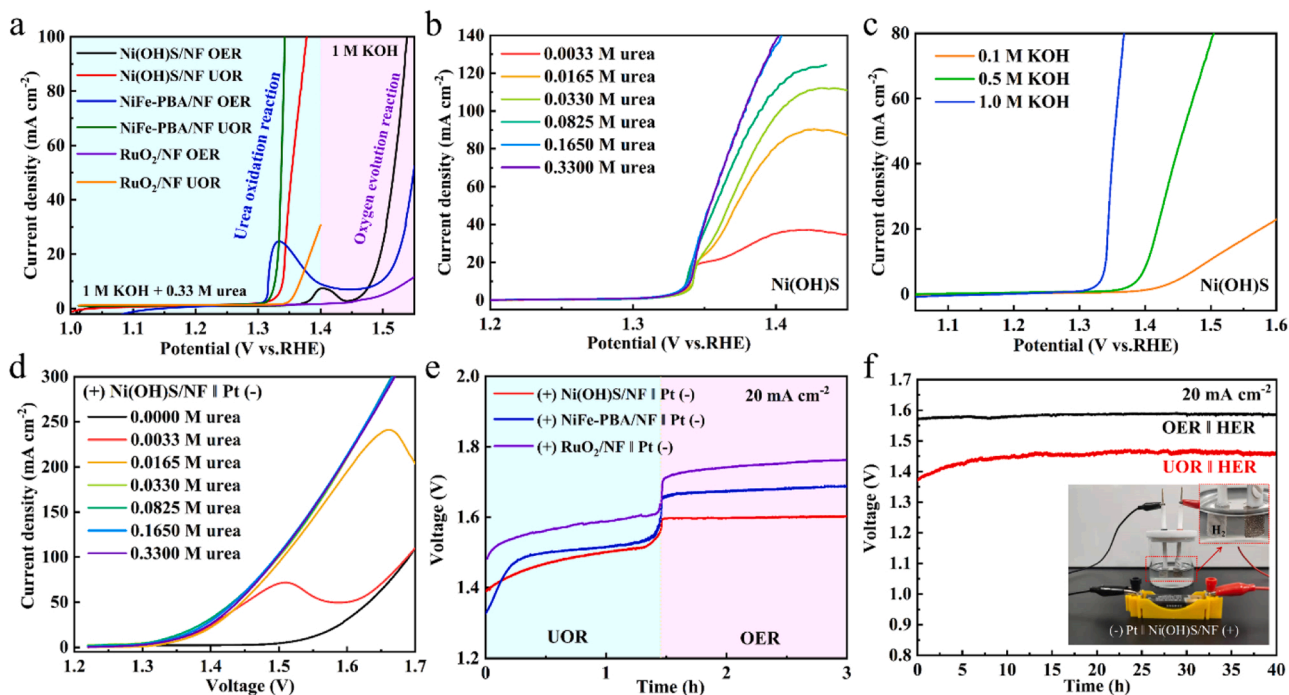


Fig. 4. (a) UOR performance of Ni(OH)S/NF, NiFe-PBA/NF, and RuO₂/NF with and without 0.33 M urea in 1.0 M KOH. (b) LSV curves of Ni(OH)S/NF in 1.0 M KOH electrolytes with different concentrations of urea. (c) LSV curves of Ni(OH)S/NF at different KOH electrolyte concentrations that contain 0.33 M urea. (d) Polarization curves of Ni(OH)S/NF||Pt for water splitting in 1.0 M KOH electrolytes with different urea concentrations. (e) The chronoamperometry curves of Ni(OH)S/NF||Pt, NiFe-PBA/NF||Pt, and RuO₂/NF||Pt at a current density of 20 mA cm⁻² in 40 mL 1.0 M KOH with 0.0165 M urea. (f) The chronoamperometry curves of Ni(OH)S/NF||Pt at the current density of 20 mA cm⁻² for 40 h with and without 0.33 M urea in 1.0 M KOH. Inset: A water electrolysis device was driven by a 1.5 V commercial battery in 1.0 M KOH with 0.33 M urea.

favorable kinetics of Ni(OH)S/NF for the OER. The low overpotential of 250 mV toward Ni(OH)S/NF is superior to some Ni-based and S-based electrocatalysts in Fig. 3c [24,41–47]. In addition, the electrochemical active surface areas (ECSA) of the Ni(OH)S catalyst were calculated based on its double-layer capacitance (C_{dl} , Fig. S9). The C_{dl} of the Ni(OH)S/NF catalysts was 6.92 mF cm^{-2} . Faradaic efficiency is also essential in evaluating the electrocatalytic OER activity by comparing the generated O_2 volumes and theoretical values (Fig. 3d). When a current density of 20 mA cm^{-2} was applied, the Faradaic efficiency of the OER on the Ni(OH)S/NF catalyst was 99.34%. In addition to OER activity, the stability of the amorphous Ni(OH)S/NF catalyst was assessed using CP tests at 20 and 50 mA cm^{-2} for 40 h (Fig. 3e). The voltage profiles clearly showed that the overpotential almost remained unchanged at 20 mA cm^{-2} and slightly increased at 50 mA cm^{-2} . The LSV curves obtained before and after the stability test displayed nearly the same overpotential. Still, the overall profile after the stability test showed more obvious high potential oxidation peaks (Fig. 3f), which indicates more Ni^{3+} active sites participating in the OER.

The UOR process, which needs to go through stepwise electrochemical oxidation and chemical oxidation processes, is different from the OER through continuous electrochemical oxidation. 0.33 M urea was chosen and added to the electrolysis because human urine contains 2–2.5 wt% urea (approximately the same as a molar concentration of $\sim 0.33 \text{ M}$). As observed in Fig. 4a, the potential of the Ni(OH)S/NF electrode displayed a negative shift with the addition of urea. The Ni(OH)S/NF showed satisfactory UOR performance with a lower potential of 1.34 V at a current density of 10 mA cm^{-2} and 1.37 V at a current density of 100 mA cm^{-2} , compared to the OER (1.53 V at 100 mA cm^{-2}). Meanwhile, it is slightly inferior to the known NiFe-PBA/NF UOR catalyst ($\sim 1.34 \text{ V}$ at 100 mA cm^{-2} , Fig. 4a), but outperforms most of the reported Ni-based UOR catalysts (Fig. S10) and the RuO_2/NF OER benchmark catalyst ($\sim 1.37 \text{ V}$ at 10 mA cm^{-2}) [16,48–54].

The kinetic study showed that the UOR process on the Ni(OH)S/NF electrode is independent of urea concentration (Fig. 4b) while strongly dependent on the amount of KOH (Fig. 4c), consistent with the other reported nickel-based electrocatalysts. The chronoamperometry tests were performed at 20 mA cm^{-2} for 20 h to evaluate the UOR stability of the Ni(OH)S/NF electrode (Fig. S11a). The catalyst stability was affected to a certain extent due to the continuous decomposition of urea molecules in a limited electrolytic cell and the generation of CO_2 on the electrodes [7]. The potential during the UOR process increased significantly in the first few hours. The LSV curves obtained before and after the stability test displayed a 20 mV increase in potential due to the possible carbon dioxide poisoning (Fig. S11b). The initial curve showed a smaller Tafel slope due to a large amount of Ni^{3+} at the beginning to trigger the UOR process. After the stability test, Ni^{3+} had been reduced to Ni^{2+} , resulting in a more significant slope. In addition, as shown in Fig. S12, the Faradaic efficiency of UOR on the Ni(OH)S/NF electrode is 99.42% at a current density of 20 mA cm^{-2} , indicating that Ni(OH)S/NF is an effective electrocatalyst for the UOR as well.

Finally, for the sake of demonstrating its potential as an anode electrocatalyst for hydrogen generation via water splitting, a full water-splitting electrolyzer was constructed by employing a Pt plate as the cathode catalyst and the as-obtained Ni(OH)S/NF as the anode catalyst in the alkaline electrolyte with different concentrations of urea. As shown in Fig. 4d, a relatively low cell voltage of 1.54 V was achieved at 10 mA cm^{-2} in 1.0 M KOH. Furthermore, it was reduced to 1.36 V with anodic UOR. However, hydrogen production at a high current density is unstable at a low concentration of urea (0.0165 M, Fig. 4d) since OER and UOR exist simultaneously. Moreover, the generation of CO_2 on the electrode affects the UOR stability of the catalyst. Therefore, to verify the stability and high efficiency of the bifunctional catalyst for hydrogen production, these Ni(OH)S/NF, NiFe-PBA/NF, and RuO_2/NF electrodes were studied in an electrolytic cell with a low concentration urea solution (40 mL 1.0 M KOH and 0.0165 M urea). As shown in Fig. 4e, the UOR occurs first and simultaneously experiences CO_2 poisoning,

resulting in a decline stability, followed by the occurrence of OER after urea consumption. Benefiting from high performance for both the OER and UOR, the Ni(OH)S/NF has the best stability with smaller power consumption under the same hydrogen production volume. Therefore, developing bifunctional catalysts with high-efficiency OER and UOR performance is significant for efficient and stable hydrogen production. Finally, hydrogen production tests up to 40 h were carried out to explore the stability of the Ni(OH)S/NF||Pt plate, as shown in Fig. 4f. The Ni(OH)S/NF||Pt hydrogen production device steadily operated for a significant period. As demonstrated in Fig. 4f, water-splitting in a urea-containing solution can be realized by using a 1.5 V battery, thereby realizing efficient hydrogen generation. Therefore, the Ni(OH)S/NF electrode exhibited beneficial OER and UOR performance compared to some previously reported representative S-based catalysts (Table 1).

3.4. Mechanistic insight into the electrocatalytic activity

Since the catalytic production of hydrogen is unstable at high current densities with a low concentration of urea, we analyze the structure-activity relationship between the potential-dependent interface behavior during OER or UOR through operando electrochemical impedance spectroscopy (EIS) and *in situ* Raman spectra [20,40]. According to Nyquist and Bode plots in 1 M KOH, there is no electrocatalytic oxidation process (Ni^{2+} to Ni^{3+}) when potentials is lower than 1.5 V, because OER only occurs in the presence of Ni(III) species. When the applied potential exceeded 1.50 V in 1 M KOH, the diameter and the phase angle reduced, confirming the OER (Fig. 5a, b). At various potentials (Fig. 5c), there is no apparent change from the Raman spectra, indicating that Ni^{3+} species always exist during the OER process. From 1.35–1.45 V in 1 M KOH with 0.33 M urea, the diameter and the phase angle also became smaller, indicating that the UOR occurred at a lower potential (Fig. 5d, e). Besides, the significant change from Raman spectra (Fig. 5f) indicates that the native Ni^{3+} ions in the Ni(OH)S trigger the UOR process. However, beyond 1.50 V, the diameter of the second semicircle and the phase angle of the low-frequency region (0.1 Hz) increase, which represents a passivation reaction [64], indicating the UOR activity of Ni(OH)S was inhibited at high potentials. In 1 M KOH with 0.0165 M urea, the diameter and the phase angle became smaller (Fig. 5g, h), and the consumption of Ni^{3+} species was also observed from Raman spectroscopy at the potential of 1.35–1.45 V (Fig. 5i), which indicates the UOR occurred. However, the Nyquist and Bode plots showed the same as OER at potentials from 1.50 to 1.60 V, and the Ni^{3+} species were accumulated after 1.50 V. This means that the

Table 1

Comparison of the OER and UOR performance between the Ni(OH)S/NF and some other representative S-based catalysts described in the literature.

Catalysts	Electrolyte	Cell voltage at 10 mA cm^{-2} (V)	Reference
Cu-Ni ₃ S ₂ /Co ₃ S ₄	1 M KOH (OER)	1.49	[55]
NiCo(OH) ₂ /NiS ₂	1 M KOH (OER)	1.49	[56]
Ni-Co ₉ S ₈ /rGN	1 M KOH (OER)	1.48	[57]
3Fe-Ni ₃ S ₂ /NF	1 M KOH (OER)	1.47	[58]
NiCoS/NF	1 M KOH (OER)	1.45	[59]
Ni@S-C-500	1 M KOH + 0.33 M urea (UOR)	1.41	[60]
Ni@NCNT	1 M KOH + 0.50 M urea (UOR)	1.38	[16]
NiMoS/NF	1 M KOH + 0.50 M urea (UOR)	1.38	[61]
W-NiS ₂ /MoO ₂ @CC	1 M KOH + 0.33 M urea (UOR)	1.37	[62]
NiSe ₂ /FeSe ₂	1 M KOH + 0.33 M urea (UOR)	1.35	[63]
Ni(OH)S/NF	1 M KOH (OER)	1.48	This work
Ni(OH)S/NF	1 M KOH + 0.33 M urea (UOR)	1.34	

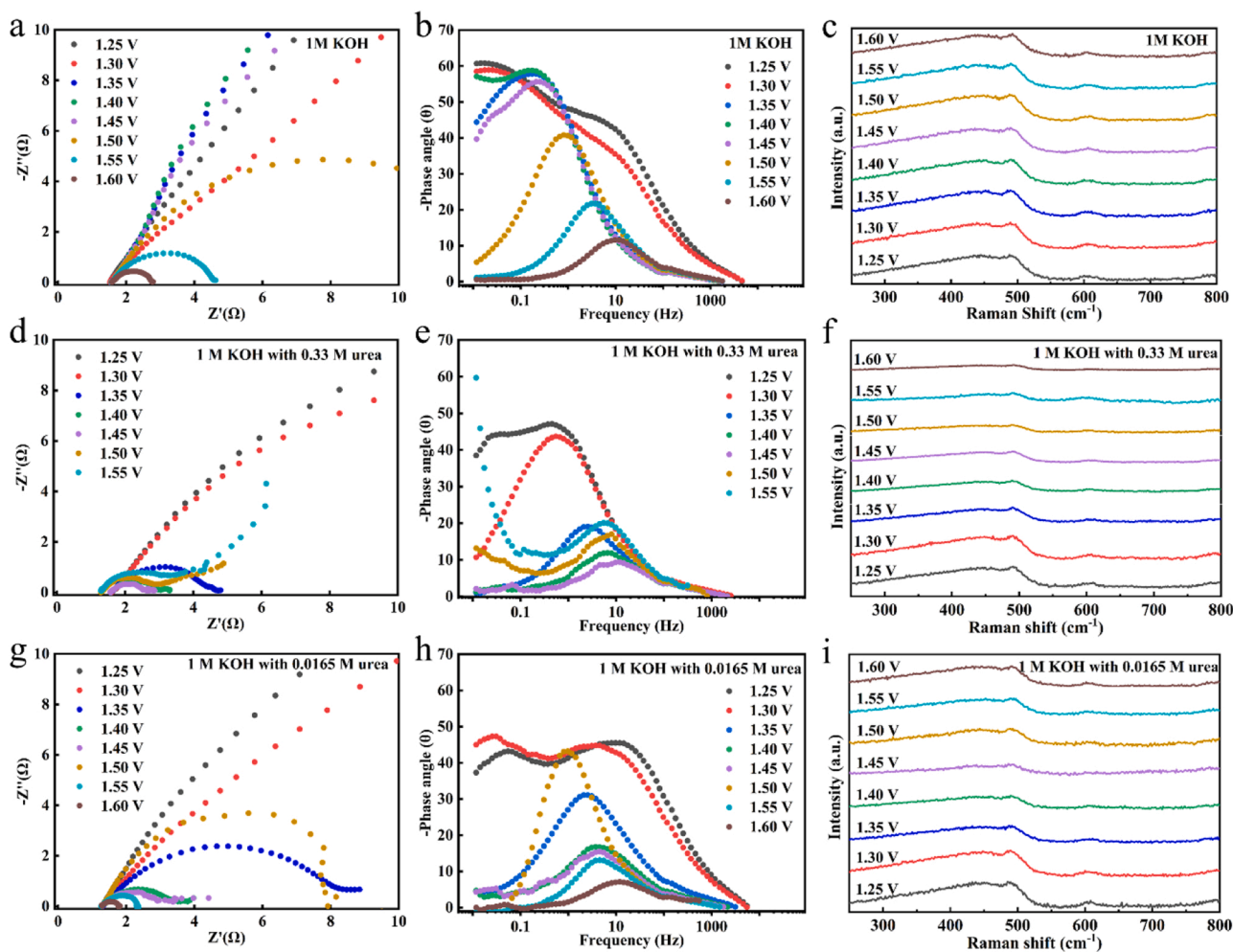


Fig. 5. Operando analysis of the intricate internal relationships among surface species and reactions to Ni(OH)S/NF during the OER or UOR. (a, d, g) Nyquist, (b, e, h) Bode plots and (c, f, i) *in situ* Raman spectra for the Ni(OH)S/NF in 1 M KOH with 0, 0.33, and 0.0165 M urea.

OER is dominant at high potential owing to the low concentration of urea and the urea supply is insufficient to trigger UOR. Overall, these findings show that developing highly efficient OER and UOR bifunctional catalysts is necessary for stable hydrogen production in wastewater with fluctuating urea concentrations.

To further elucidate the changes of Ni(OH)S during the OER and the UOR, and provide insight into the relevant mechanisms, various spectroscopic measurements after the stability tests of OER and UOR were carried out. For the OER, FT-IR was employed (Fig. S13) after the stability tests. There are many new peaks in the FT-IR spectrum, where the new infrared absorption bands at 634, 984, 1153, and 1239 cm^{-1} could be ascribed to the sulfate ion (SO_4^{2-}), and the band at 1059 cm^{-1} could be assigned to superoxide species (O_2^-) [65]. The XPS analysis of the Ni(OH)S after the OER (Fig. S14) revealed that the atomic content of S decreased from 9.56% to 1.81%, and the S/Ni ratio decreased from 2.16 to 0.06. Furthermore, in the S 1p XPS spectra, the S-Ni chemical bond was weakened after OER, but the S-O chemical bond was significantly enhanced. These results showed that the sulfur content is considerably reduced after OER and mainly exists in SO_4^{2-} . Therefore, Ni(OH)S acts as a precursor for OER, which can be reconstructed to NiOOH as the active site for catalytic OER under alkaline conditions. In addition, the electron binding energy of Ni 2p_{3/2} shifts to higher energy ($\Delta E = 0.4$ eV), indicating the change of the chemical environment at the Ni center, and Ni^{3+} was transformed into Ni^{4+} . Combined with the generation of the superoxide intermediates, this provides direct evidence to uncover the OER catalytic mechanisms. The active phase NiOOH has a similar role to

the metal-porphyrins or porphyrin-like molecular catalysts (Fig. 6a). The whole reaction consists of four steps as follows. The first step is the deprotonation of the surface-adsorbed OH⁻ on Ni, converting the surface $\text{Ni}^{3+}\text{-OH}$ group into $\text{Ni}^{3+}\text{-O}^-$. Subsequently, this O-radical is further deprotonated by OH⁻ to yield superoxide $^{\bullet}\text{OOH}$, accompanied by the oxidation of Ni^{3+} into Ni^{4+} to form a superoxide $\text{Ni}^{4+}\text{-OOH}$ intermediate (step II). After that, the superoxide OOH species is further deprotonated into O_2 -radical (step III). The fourth proton-coupling electron transfer (step IV) leads to further oxidation of O_2 -radical to release an O_2 molecule. Then the desorption of OH⁻ from the Ni sites restores them to the original state of $\text{Ni}^{3+}\text{-OH}$.

For the UOR, similar to the OER, the FT-IR spectrum of Ni(OH)S showed that sulfur also existed in the form of SO_4^{2-} after UOR (Fig. S15). The XPS analysis of the Ni(OH)S after the UOR (Fig. S16) also revealed that the atomic content of S decreased from 9.56% to 2.11%, and the S/Ni ratio decreased from 2.16 to 0.28. Moreover, in the S 1p XPS spectra also found that the S-Ni chemical bond weakened, and the S-O chemical bond enhanced significantly after UOR. Therefore, the Ni(OH)S also acts as a precursor for the UOR. However, unlike OER, the electron binding energy of Ni 2p_{3/2} shifts to lower energy, indicating the change of the chemical environment at the Ni center, and Ni^{3+} was transformed into Ni^{2+} . The Raman spectra of Ni(OH)S in the UOR process also showed the disappearance of the Ni^{3+} peak (Fig. 5f). Based on these results, the UOR mechanism of Ni(OH)S can be proposed (Fig. 6b). Ni(OH)S is first completely reconstructed to NiOOH, and then the active phase (NiOOH) is converted to Ni(OH)_2 to realize the decomposition of urea. The XPS

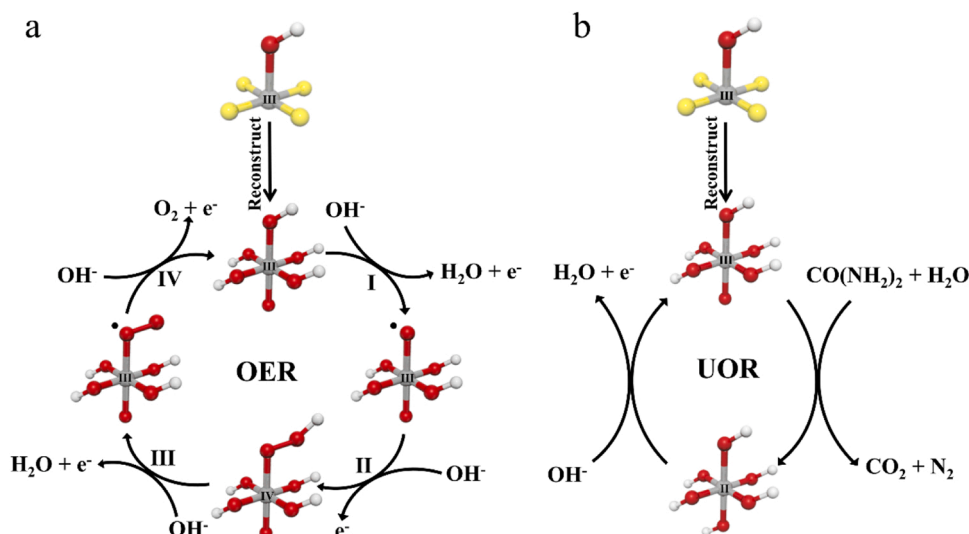


Fig. 6. Proposed catalytic mechanisms for (a) the OER and (b) the UOR on the Ni(OH)S catalyst.

analysis of the Ni(OH)S after UOR (Fig. S16) showed that the atomic content of N increased to 4.93%, and the N-H, N-C, and N-O species in the *N 1s* XPS spectra were found, indicating the decomposition of urea. The UOR usually has three oxidation pathways: $\text{CO}(\text{NH}_2)_2 + 8\text{OH}^- \rightarrow \text{N}_2 + \text{CO}_3^{2-} + 5\text{H}_2\text{O} + 6\text{e}^-$; $\text{CO}(\text{NH}_2)_2 + 16\text{OH}^- \rightarrow 2\text{NO}_2^- + \text{CO}_3^{2-} + 10\text{H}_2\text{O} + 12\text{e}^-$; $\text{CO}(\text{NH}_2)_2 + 20\text{OH}^- \rightarrow 2\text{NO}_3^- + \text{CO}_3^{2-} + 12\text{H}_2\text{O} + 16\text{e}^-$ [66]. The few N-O species in *N 1s* XPS spectra were indicating the UOR pathway on the Ni(OH)S maybe $^*\text{CO}(\text{NH}_2)_2 \rightarrow ^*\text{CO}(\text{NH}\cdot\text{NH}_2) \rightarrow ^*\text{CO}(\text{NH}\cdot\text{NH}) \rightarrow ^*\text{CO}(\text{NH}\cdot\text{N}) \rightarrow ^*\text{CO}(\text{N}_2) \rightarrow ^*\text{CO}(\text{OH}) + \text{N}_2 \rightarrow ^*\text{CO}(\text{OH}\cdot\text{OH}) \rightarrow ^*\text{COO}$.

Therefore, the superior performance of the Ni(OH)S for the OER and UOR could be attributed to their structure and compositional benefits. The amorphous phase of Ni(OH)S with abundant defects could reduce the required energy for the distortion of the active site. Moreover, S has higher polarization ability and lower electronegativity than O [67]. These features of the Ni(OH)S catalyst facilitate the entire transformation of originally inert species into the active phase during OER and UOR process [29]. In addition, S provides more electrons to the Ni cations and delocalizes their *d*-electrons, which reduces the strength of the bond between the catalyst and the various oxygen-containing intermediates ($^*\text{O}$, $^*\text{COO}$, etc.) produced during the OER and UOR [68], facilitating the final desorption process during the OER and UOR. Furthermore, favorable adsorption sites for reaction intermediates originated from the amorphous phase and the electronic configuration of $t_{2g}^6 e_g^1$ of Ni^{3+} , thus boosting OER activity. Besides, the inherent oxidation state of Ni^{3+} leads to a more efficient UOR.

4. Conclusions

In summary, a high-efficiency and low-cost bifunctional OER/UOR electrocatalyst containing noble-metal-free Ni and S-based amorphous structure was developed by an efficient and facile synthesis method. From spectroscopic characterizations and DFT calculation results, the *in situ* synthesized amorphous Ni(OH)S via hydrolysis of $\text{NiCl}_2(\text{CH}_3\text{CSNH}_2)_4$ is a Ni^{3+} -enriched phase. Benefiting from the amorphous structural and Ni^{3+} phase, the electrocatalyst exhibited excellent OER and UOR activities with low overpotential, low Tafel slopes, along with encouraging stability in alkaline media. Compared to UOR and OER catalysts with a single functional catalytic performance, the Ni(OH)S/NF electrode showed the least power consumption under the same hydrogen production volume. Moreover, the reaction interface between OER and UOR was effectively identified by operando EIS and *in-situ* Raman spectroscopy, which verified the necessity and promising possibility of developing OER and UOR bifunctional catalysts. Overall,

the novel strategy guides in designing high-performance electrocatalysts for challenging bifunctional OER/UOR applications and opens a new approach for efficient and stable hydrogen production via water splitting.

CRediT authorship contribution statement

Xin Jia, Hongjun Kang, Xiaoxuan Yang, and Yunlong Li: catalyst synthesis, electrochemical measurements, and materials characterization. Kai Cui carried out DFT calculations. Xiaohong Wu, Wei Qin, and Gang Wu: proposed the new concept and design experiments; data analysis and discussion; manuscript writing.

Declaration of Competing Interest

The authors declare that they have no known competing financial interests or personal relationships that could have appeared to influence the work reported in this paper.

Acknowledgments

W. Q. and X.H. W. thank the financial support from the National Natural Science Foundation of China (Grant No. U2067216, U2130109, and 51902070). H.J. K. acknowledges the China Postdoctoral Science Foundation (2020M670904). G. W. thanks the support from the University at Buffalo, the State University of New York.

Appendix A. Supporting information

Supplementary data associated with this article can be found in the online version at doi:10.1016/j.apcatb.2022.121389.

References

- [1] N. Mahmood, Y. Yao, J.-W. Zhang, L. Pan, X. Zhang, J.-J. Zou, Electrocatalysts for hydrogen evolution in alkaline electrolytes: mechanisms, challenges, and prospective solutions, *Adv. Sci.* 5 (2018), 1700464, <https://doi.org/10.1002/advs.201700464>.
- [2] Y. Li, H. Wang, C. Priest, S. Li, P. Xu, G. Wu, Advanced electrocatalysis for energy and environmental sustainability via water and nitrogen reactions, *Adv. Mater.* 33 (2021), 2000381.
- [3] B.M. Hunter, H.B. Gray, A.M. Müller, Earth-abundant heterogeneous water oxidation catalysts, *Chem. Rev.* 116 (2016) 14120–14136, <https://doi.org/10.1021/acs.chemrev.6b00398>.
- [4] C. Li, Y. Liu, Z. Zhuo, H. Ju, D. Li, Y. Guo, X. Wu, H. Li, T. Zhai, Local charge distribution engineered by schottky heterojunctions toward urea electrolysis, *Adv. Energy Mater.* 8 (2018), 1801775, <https://doi.org/10.1002/aenm.201801775>.

- [5] M. Song, Z. Zhang, Q. Li, W. Jin, Z. Wu, G. Fu, X. Liu, Ni-foam supported Co(OH)F and Co-P nanoarrays for energy-efficient hydrogen production via urea electrolysis, *J. Mater. Chem. A* 7 (2019) 3697–3703, <https://doi.org/10.1039/C8TA10985K>.
- [6] J. Zhang, F. Xing, H. Zhang, Y. Huang, Ultrafine NiFe clusters anchored on N-doped carbon as bifunctional electrocatalysts for efficient water and urea oxidation, *Dalton Trans.* 49 (2020) 13962–13969, <https://doi.org/10.1039/D0DT02459G>.
- [7] X. Zhu, X. Dou, J. Dai, X. An, Y. Guo, L. Zhang, S. Tao, J. Zhao, W. Chu, X.C. Zeng, C. Wu, Y. Xie, Metallic nickel hydroxide nanosheets give superior electrocatalytic oxidation of urea for fuel cells, *Angew. Chem. Int. Ed.* 55 (2016) 12465–12469, <https://doi.org/10.1002/anie.201606313>.
- [8] Z. Wang, W. Liu, Y. Hu, M. Guan, L. Xu, H. Li, J. Bao, H. Li, Cr-doped CoFe layered double hydroxides: highly efficient and robust bifunctional electrocatalyst for the oxidation of water and urea, *Appl. Catal. B Environ.* 272 (2020), 118959, <https://doi.org/10.1016/j.apcatb.2020.118959>.
- [9] Y. He, G. Wu, PGM-free oxygen-reduction catalyst development for proton-exchange membrane fuel cells: challenges, solutions, and promises, *Acc. Mater. Res.* 3 (2022) 224–236.
- [10] Y. He, X. Yang, Y. Li, L. Liu, S. Guo, C. Shu, F. Liu, Y. Liu, Q. Tan, G. Wu, Atomically dispersed Fe-Co dual metal sites as bifunctional oxygen electrocatalysts for rechargeable and flexible Zn-Air batteries, *ACS Catal.* 12 (2022) 1216–1227.
- [11] X. Zhou, X. Liu, J. Zhang, C. Zhang, S.J. Yoo, J.-G. Kim, X. Chu, C. Song, P. Wang, Z. Zhao, D. Li, W. Zhang, W. Zheng, Highly-dispersed cobalt clusters decorated onto nitrogen-doped carbon nanotubes as multifunctional electrocatalysts for OER, HER and ORR, *Carbon* 166 (2020) 284–290, <https://doi.org/10.1016/j.carbon.2020.05.037>.
- [12] C. Zhang, W. Zhang, N.E. Drewett, X. Zhang, S.J. Yoo, H. Wang, T. Deng, J.-G. Kim, H. Chen, K. Huang, S. Feng, W. Zheng, Integrating catalysis of methane decomposition and electrocatalytic hydrogen evolution with Ni/CeO₂ for improved hydrogen production efficiency, *ChemSusChem* 12 (2019) 1000–1010, <https://doi.org/10.1002/cssc.201802618>.
- [13] C. Zhang, H. Nan, H. Tian, W. Zheng, Recent advances in pentlandites for electrochemical water splitting: A short review, *J. Alloy. Compd.* 838 (2020), 155685, <https://doi.org/10.1016/j.jallcom.2020.155685>.
- [14] H. Osgood, S.V. Devaguptapu, H. Xu, J.P. Cho, G. Wu, Transition metal (Fe, Co, Ni, and Mn) oxides for oxygen reduction and evolution bifunctional catalysts in alkaline media, *Nano Today* 11 (2016) 601–625.
- [15] G. Gnana kumar, A. Farithkhan, A. Manthiram, Direct urea fuel cells: recent progress and critical challenges of urea oxidation electrocatalysis, *Adv. Energy Sustain. Res.* 1 (2020), 2000015, <https://doi.org/10.1002/aesr.202000015>.
- [16] Q. Zhang, F.M.D. Kazim, S. Ma, K. Qu, M. Li, Y. Wang, H. Hu, W. Cai, Z. Yang, Nitrogen dopants in nickel nanoparticles embedded carbon nanotubes promote overall urea oxidation, *Appl. Catal. B Environ.* 280 (2021), 119436, <https://doi.org/10.1016/j.apcatb.2020.119436>.
- [17] J. Song, C. Wei, Z.-F. Huang, C. Liu, L. Zeng, X. Wang, Z.J. Xu, A review on fundamentals for designing oxygen evolution electrocatalysts, *Chem. Soc. Rev.* 49 (2020) 2196–2214, <https://doi.org/10.1039/C9CS00607A>.
- [18] J. Wang, Y. Gao, D. Chen, J. Liu, Z. Zhang, Z. Shao, F. Ciucci, Water splitting with an enhanced bifunctional double perovskite, *ACS Catal.* 8 (2018) 364–371, <https://doi.org/10.1021/acscatal.7b02650>.
- [19] J. Huang, J. Chen, T. Yao, J. He, S. Jiang, Z. Sun, Q. Liu, W. Cheng, F. Hu, Y. Jiang, Z. Pan, S. Wei, CoOOH nanosheets with high mass activity for water oxidation, *Angew. Chem. Int. Ed.* 54 (2015) 8722–8727, <https://doi.org/10.1002/ange.201502836>.
- [20] W. Chen, L. Xu, X. Zhu, Y.-C. Huang, W. Zhou, D. Wang, Y. Zhou, S. Du, Q. Li, C. Xie, L. Tao, C.-L. Dong, J. Liu, Y. Wang, R. Chen, H. Su, C. Chen, Y. Zou, Y. Li, Q. Liu, S. Wang, Unveiling the electrooxidation of urea: intramolecular coupling of the N–N bond, *Angew. Chem. Int. Ed.* 60 (2021) 7297–7307, <https://doi.org/10.1002/anie.202015773>.
- [21] D. Wang, S. Liu, Q. Gan, J. Tian, T.T. Isimjan, X. Yang, Two-dimensional nickel hydroxide nanosheets with high-content of nickel(III) species towards superior urea electro-oxidation, *J. Electroanal. Chem.* 829 (2018) 81–87, <https://doi.org/10.1016/j.jelechem.2018.10.007>.
- [22] R.P. Forslund, J.T. Mefford, W.G. Hardin, C.T. Alexander, K.P. Johnston, K. J. Stevenson, Nanostructured LaNiO₃ perovskite electrocatalyst for enhanced urea oxidation, *ACS Catal.* 6 (2016) 5044–5051, <https://doi.org/10.1021/acscatal.6b00487>.
- [23] Z.-Y. Yu, C.-C. Lang, M.-R. Gao, Y. Chen, Q.-Q. Fu, Y. Duan, S.-H. Yu, Ni–Mo–O nanorod-derived composite catalysts for efficient alkaline water-to-hydrogen conversion via urea electrolysis, *Energy Environ. Sci.* 11 (2018) 1890–1897, <https://doi.org/10.1039/C8EE00521D>.
- [24] K. Wan, J. Luo, C. Zhou, T. Zhang, J. Arbiol, X. Lu, B.-W. Mao, X. Zhang, J. Fransaer, Hierarchical porous Ni₃S₄ with enriched high-valence Ni sites as a robust electrocatalyst for efficient oxygen evolution reaction, *Adv. Funct. Mater.* 29 (2019), 1900315, <https://doi.org/10.1002/adfm.201900315>.
- [25] J. Huang, Y. Li, Y. Zhang, G. Rao, C. Wu, Y. Hu, X. Wang, R. Lu, Y. Li, J. Xiong, Identification of key reversible intermediates in self-reconstructed nickel-based hybrid electrocatalysts for oxygen evolution, *Angew. Chem. Int. Ed.* 58 (2019) 17458–17464, <https://doi.org/10.1002/anie.201910716>.
- [26] Y. Jiao, W. Hong, P. Li, L. Wang, G. Chen, Metal-organic framework derived Ni/NiO micro-particles with subtle lattice distortions for high-performance electrocatalyst and supercapacitor, *Appl. Catal. B: Environ.* 244 (2019) 732–739, <https://doi.org/10.1016/j.apcatb.2018.11.035>.
- [27] Y. Tong, Y. Guo, P. Chen, H. Liu, M. Zhang, L. Zhang, W. Yan, W. Chu, C. Wu, Y. Xie, Spin-state regulation of perovskite cobaltite to realize enhanced oxygen evolution activity, *Chem* 3 (2017) 812–821, <https://doi.org/10.1016/j.chempr.2017.09.003>.
- [28] Y. Liu, X. Hua, C. Xiao, T. Zhou, P. Huang, Z. Guo, B. Pan, Y. Xie, Heterogeneous spin states in ultrathin nanosheets induce subtle lattice distortion to trigger efficient hydrogen evolution, *J. Am. Chem. Soc.* 138 (2016) 5087–5092, <https://doi.org/10.1021/jacs.6b00858>.
- [29] A. Sivanantham, P. Ganesan, A. Vinu, S. Shanmugam, Surface activation and reconstruction of non-oxide-based catalysts through in situ electrochemical tuning for oxygen evolution reactions in alkaline media, *ACS Catal.* 10 (2020) 463–493, <https://doi.org/10.1021/acscatal.9b04216>.
- [30] X. Shang, B. Dong, Y.-M. Chai, C.-G. Liu, In-situ electrochemical activation designed hybrid electrocatalysts for water electrolysis, *Sci. Bull.* 63 (2018) 853–876, <https://doi.org/10.1016/j.scib.2018.05.014>.
- [31] J. Kwon, H. Han, S. Jo, S. Choi, K.Y. Chung, G. Ali, K. Park, U. Paik, T. Song, Amorphous nickel-iron borophosphate for a robust and efficient oxygen evolution reaction, *Adv. Energy Mater.* 11 (2021), 2100624, <https://doi.org/10.1002/aenm.202100624>.
- [32] R.L. Girling, J.E. O'Connor, E.L. Amma, The crystal and molecular structure of trans-dichlorotetrakis(thioacetamido)nickel(II), *Acta Crystallogr. Sect. B* 28 (1972) 2640–2647, <https://doi.org/10.1107/S0567740872006703>.
- [33] M. Guo, A. Qayum, S. Dong, X. Jiao, D. Chen, T. Wang, In situ conversion of metal (Ni, Co or Fe) foams into metal sulfide (Ni₃S₂, Co₉S₈ or FeS) foams with surface grown N-doped carbon nanotube arrays as efficient superhydrophobic electrocatalysts for overall water splitting, *J. Mater. Chem. A* 8 (2020) 9239–9247, <https://doi.org/10.1039/D0TA02337J>.
- [34] A. Sivanantham, P. Ganesan, S. Shanmugam, Bifunctional electrocatalysts: hierarchical NiCo₂S₄ nanowire arrays supported on Ni Foam: an efficient and durable bifunctional electrocatalyst for oxygen and hydrogen evolution reactions (Adv. Funct. Mater. 26(2016), Adv. Funct. Mater. 26 (2016), <https://doi.org/10.1002/adfm.201670166>.
- [35] B. Konkena, J. Masa, A.J.R. Botz, I. Sinev, W. Xia, J. Kößmann, R. Drautz, M. Muhler, W. Schuhmann, Metallic NiPS₃@NiOOH core-shell heterostructures as highly efficient and stable electrocatalyst for the oxygen evolution reaction, *ACS Catal.* 7 (2017) 229–237, <https://doi.org/10.1021/acscatal.6b02203>.
- [36] M. Steimecke, G. Seiffarth, C. Schneemann, F. Oehler, S. Förster, M. Bron, Higher-valent nickel oxides with improved oxygen evolution activity and stability in alkaline media prepared by high-temperature treatment of Ni(OH)₂, *ACS Catal.* 10 (2020) 3595–3603, <https://doi.org/10.1021/acscatal.9b04788>.
- [37] C. Cui, J. Wang, Z. Luo, J. Wang, C. Li, Z. Li, MOF-mediated synthesis of monodisperse Co(OH)₂ flower-like nanosheets for enhanced oxygen evolution reaction, *Electrochim. Acta* 273 (2018) 327–334, <https://doi.org/10.1016/j.electacta.2018.04.016>.
- [38] M. Zhang, M. de Respinis, H. Frei, Time-resolved observations of water oxidation intermediates on a cobalt oxide nanoparticle catalyst, *Nat. Chem.* 6 (2014) 362–367, <https://doi.org/10.1038/nchem.1874>.
- [39] J. Zhang, Q. Kong, L. Yang, D.-Y. Wang, Few layered Co(OH)₂ ultrathin nanosheet-based polyurethane nanocomposites with reduced fire hazard: from eco-friendly flame retardance to sustainable recycling, *Green. Chem.* 18 (2016) 3066–3074, <https://doi.org/10.1039/C5GC03048J>.
- [40] S.-K. Geng, Y. Zheng, S.-Q. Li, H. Su, X. Zhao, J. Hu, H.-B. Shu, M. Jaroniec, P. Chen, Q.-H. Liu, S.-Z. Qiao, Nickel ferrocyanide as a high-performance urea oxidation electrocatalyst, *Nat. Energy* 6 (2021) 904–912, <https://doi.org/10.1038/s41560-021-00899-2>.
- [41] J.S. Chen, J. Ren, M. Shalom, T. Feller, M. Antonietti, Stainless steel mesh-supported NiS nanosheet array as highly efficient catalyst for oxygen evolution reaction, *ACS Appl. Mater. Interfaces* 8 (2016) 5509–5516, <https://doi.org/10.1021/acsaami.5b10099>.
- [42] J.-T. Ren, Z.-Y. Yuan, Hierarchical nickel sulfide nanosheets directly grown on Ni foam: a stable and efficient electrocatalyst for water reduction and oxidation in alkaline medium, *ACS Sustain. Chem. Eng.* 5 (2017) 7203–7210, <https://doi.org/10.1021/acssuschemeng.7b01419>.
- [43] J. Wang, H.C. Zeng, A hybrid electrocatalyst with a coordinatively unsaturated metal-organic framework shell and hollow Ni₃S₂/NiS core for oxygen evolution reaction applications, *ACS Appl. Mater. Interfaces* 11 (2019) 23180–23191, <https://doi.org/10.1021/acsaami.9b04479>.
- [44] W. Xiang, Q. Tian, C. Zhong, Y. Deng, X. Han, W. Hu, A Solution-based Method for Synthesizing Pyrite-type Ferrous Metal Sulfide Microspheres with Efficient OER Activity, *Chem. – Asian J.* 15 (2020) 2231–2238, <https://doi.org/10.1002/asia.202000504>.
- [45] S. Ju, Y. Liu, H. Chen, F. Tan, A. Yuan, X. Li, G. Zhu, In situ surface chemistry engineering of cobalt-sulfide nanosheets for improved oxygen evolution activity, *ACS Appl. Energy Mater.* 2 (2019) 4439–4449, <https://doi.org/10.1021/acsaem.9b00687>.
- [46] P. Luo, H. Zhang, L. Liu, Y. Zhang, J. Deng, C. Xu, N. Hu, Y. Wang, Targeted synthesis of unique nickel sulfide (NiS, NiS₂) microarchitectures and the applications for the enhanced water splitting system, *ACS Appl. Mater. Interfaces* 9 (2017) 2500–2508, <https://doi.org/10.1021/acsaami.6b13984>.
- [47] H.D. Mai, V.C.T. Le, H. Yoo, Effective fabrication and electrochemical oxygen evolution reaction activity of gold multipod nanoparticle core-cobalt sulfide shell nanohybrids, *ACS Appl. Nano Mater.* 2 (2019) 678–688, <https://doi.org/10.1021/acsaanm.8b01689>.
- [48] Y. He, H. Guo, S. Hwang, X. Yang, Z. He, J. Braaten, S. Karakalos, W. Shan, M. Wang, H. Zhou, Z. Feng, K.L. More, G. Wang, D. Su, D.A. Cullen, L. Fei, S. Litter, G. Wu, Single cobalt sites dispersed in hierarchically porous nanofiber networks for durable and high-power PGM-free cathodes in fuel cells, *Adv. Mater.* 32 (2020), e2003577, <https://doi.org/10.1002/adma.202003577>.

- [49] M.-S. Wu, R.-Y. Ji, Y.-R. Zheng, Nickel hydroxide electrode with a monolayer of nanocup arrays as an effective electrocatalyst for enhanced electrolysis of urea, *Electrochim. Acta* 144 (2014) 194–199, <https://doi.org/10.1016/j.electacta.2014.08.098>.
- [50] X. Zhang, Y. Liu, Q. Xiong, G. Liu, C. Zhao, G. Wang, Y. Zhang, H. Zhang, H. Zhao, Vapour-phase hydrothermal synthesis of Ni₂P nanocrystallines on carbon fiber cloth for high-efficiency H₂ production and simultaneous urea decomposition, *Electrochim. Acta* 254 (2017) 44–49, <https://doi.org/10.1016/j.electacta.2017.09.097>.
- [51] M. He, C. Feng, T. Liao, S. Hu, H. Wu, Z. Sun, Low-Cost Ni₂P/Ni_{0.96}S heterostructured bifunctional electrocatalyst toward highly efficient overall urea-water electrolysis, *ACS Appl. Mater. Interfaces* 12 (2020) 2225–2233, <https://doi.org/10.1021/acsami.9b14350>.
- [52] W. Zhu, Z. Yue, W. Zhang, N. Hu, Z. Luo, M. Ren, Z. Xu, Z. Wei, Y. Suo, J. Wang, Wet-chemistry topotactic synthesis of bimetallic iron–nickel sulfide nanoarrays: an advanced and versatile catalyst for energy efficient overall water and urea electrolysis, *J. Mater. Chem. A* 6 (2018) 4346–4353, <https://doi.org/10.1039/C7TA10584C>.
- [53] W. Song, M. Xu, X. Teng, Y. Niu, S. Gong, X. Liu, X. He, Z. Chen, Construction of self-supporting, hierarchically structured caterpillar-like NiCo₂S₄ arrays as an efficient trifunctional electrocatalyst for water and urea electrolysis, *Nanoscale* 13 (2021) 1680–1688, <https://doi.org/10.1039/D0NR08395J>.
- [54] D. Wang, W. Yan, S.H. Vijapur, G.G. Botte, Electrochemically reduced graphene oxide–nickel nanocomposites for urea electrolysis, *Electrochim. Acta* 89 (2013) 732–736, <https://doi.org/10.1016/j.electacta.2012.11.046>.
- [55] H. Su, S. Song, S. Li, Y. Gao, L. Ge, W. Song, T. Ma, J. Liu, High-valent bimetal Ni₃S₂/Co₃S₄ induced by Cu doping for bifunctional electrocatalytic water splitting, *Appl. Catal. B: Environ.* 293 (2021), 120225, <https://doi.org/10.1016/j.apcatb.2021.120225>.
- [56] J. Wang, A. Yang, J. Li, K. Su, Y. Tang, X. Qiu, Top-down and facet-selective phase-segregation to construct concave nanocages with strongly coupled hetero-interface for oxygen evolution reaction, *Appl. Catal. B Environ.* 300 (2022), 120727, <https://doi.org/10.1016/j.apcatb.2021.120727>.
- [57] J. Wang, J. Xu, X. Guo, T. Shen, C. Xuan, B. Tian, Z. Wen, Y. Zhu, D. Wang, Synergistic regulation of nickel doping/hierarchical structure in cobalt sulfide for high performance zinc-air battery, *Appl. Catal. B Environ.* 298 (2021), 120539, <https://doi.org/10.1016/j.apcatb.2021.120539>.
- [58] Q. Chen, L. Huang, Q. Kong, X. An, X. Wu, W. Yao, C. Sun, Facile synthesis of self support Fe doped Ni₃S₂ nanosheet arrays for high performance alkaline oxygen evolution, *J. Electroanal. Chem.* 907 (2022), 116047, <https://doi.org/10.1016/j.jelechem.2022.116047>.
- [59] C. Wang, M. Zhu, Z. Cao, P. Zhu, Y. Cao, X. Xu, C. Xu, Z. Yin, Heterogeneous bimetallic sulfides based seawater electrolysis towards stable industrial-level large current density, *Appl. Catal. B: Environ.* 291 (2021), 120071, <https://doi.org/10.1016/j.apcatb.2021.120071>.
- [60] N. Wu, X. Zhang, R. Guo, M. Ma, Y. Zhang, T. Hu, Nickel nanocrystal/sulfur-doped carbon composites as efficient and stable electrocatalysts for urea oxidation reaction, *J. Alloy. Compd.* 903 (2022), 163916, <https://doi.org/10.1016/j.jallcom.2022.163916>.
- [61] F. Wang, K. Zhang, Q. Zha, Y. Ni, Honeycomb-like Ni–Mo–S on Ni foam as superior bifunctional electrocatalyst for hydrogen evolution and urea oxidation, *J. Alloy. Compd.* 899 (2022), 163346, <https://doi.org/10.1016/j.jallcom.2021.163346>.
- [62] S. Liganí Fereja, P. Li, Z. Zhang, J. Guo, Z. Fang, Z. Li, S. He, W. Chen, W-doping induced abundant active sites in a 3D NiS₂/MoO₃ heterostructure as an efficient electrocatalyst for urea oxidation and hydrogen evolution reaction, *Chem. Eng. J.* 432 (2022), 134274, <https://doi.org/10.1016/j.cej.2021.134274>.
- [63] S. Ni, H. Qu, Z. Xu, X. Zhu, H. Xing, L. Wang, J. Yu, H. Liu, C. Chen, L. Yang, Interfacial engineering of the NiSe₂/FeSe₂ p-p heterojunction for promoting oxygen evolution reaction and electrocatalytic urea oxidation, *Appl. Catal. B: Environ.* 299 (2021), 120638, <https://doi.org/10.1016/j.apcatb.2021.120638>.
- [64] G. Rondelli, P. Torricelli, M. Fini, R. Giardino, In vitro corrosion study by EIS of a nickel-free stainless steel for orthopaedic applications, *Biomaterials* 26 (2005) 739–744, <https://doi.org/10.1016/j.biomaterials.2004.03.012>.
- [65] W. Cheng, X. Zhao, H. Su, F. Tang, W. Che, H. Zhang, Q. Liu, Lattice-strained metal–organic-framework arrays for bifunctional oxygen electrocatalysis, *Nat. Energy* 4 (2019) 115–122, <https://doi.org/10.1038/s41560-018-0308-8>.
- [66] J. Li, J. Li, T. Liu, L. Chen, Y. Li, H. Wang, X. Chen, M. Gong, Z.-P. Liu, X. Yang, Inside back cover: deciphering and suppressing over-oxidized nitrogen in nickel-catalyzed urea electrolysis (*Angew. Chem. Int. Ed.* 51/2021), *Angew. Chem. Int. Ed.* 60 (2021), <https://doi.org/10.1002/anie.202114404>.
- [67] T. Wang, G. Nam, Y. Jin, X. Wang, P. Ren, M.G. Kim, J. Liang, X. Wen, H. Jang, J. Han, Y. Huang, Q. Li, J. Cho, NiFe (Oxy) hydroxides derived from nife disulfides as an efficient oxygen evolution catalyst for rechargeable Zn–Air batteries: the effect of surface S residues, *Adv. Mater.* 30 (2018), 1800757, <https://doi.org/10.1002/adma.201800757>.
- [68] X. Qiao, H. Kang, J. Wu, Y. Li, Q. Wang, X. Jia, Y. Qiao, S. Lu, X. Wu, W. Qin, A partial sulfidation approach that significantly enhance the activity of FeCo layered double hydroxide for oxygen evolution reaction, *Int. J. Hydrog. Energy* 44 (2019) 31987–31994, <https://doi.org/10.1016/j.ijhydene.2019.10.082>.